Mechanics of Materials 148 (2020) 103443

Contents lists available at ScienceDirect

Mechanics of Materials

journal homepage: www.elsevier.com/locate/mechmat

Time-dependent Mechanical Response at the Nanoscale

Juan Camilo Múnera[a], Debkalpa Goswami[b], Ramses V. Martinez[b,c], E. Alex Ossa[a,*]

[a] Department of Production Engineering, Universidad EAFIT, Cra 49, No. 7 sur 50, Medellín, Colombia
[b] School of Industrial Engineering, Purdue University, 315 N. Grant Street, West Lafayette, Indiana, 47907, United States
[c] Weldon School of Biomedical Engineering, Purdue University, 206 S. Martin Jischke Drive, West Lafayette, Indiana, 47907, United States

ARTICLE INFO

Keywords:
Time-dependent deformation
AFM
nanoindentation
Creeping solids
Nanolayers
Nanomechanics

ABSTRACT

Modern nanofabrication processes on metals, polymers, and ceramics often require deforming these materials at strain rates ranging $\sim 10^1 - 10^7\ s^{-1}$. Therefore, there is a need to develop an appropriate methodology capable of measuring and predicting the effects of these deformation rates on the final mechanical response of the nanomaterial being processed. Here we report an experimental study of the indentation response of three materials with different nature and mechanical properties, but with known time-dependent mechanical responses. These materials allow validation of the findings under a wide variety of conditions. One metal (Pb), and two polymers (PMMA and PS), were indented at the sub-20 nm scale using commercial atomic force microscopy (AFM) probes. Based on our experimental findings, we also propose an analytical model for creeping solids in which their nanoscale mechanical behavior is completely described by two components: an elastic component (characterized by the Hertz contact model) and a time-dependent component (characterized by a power-law model). The proposed experimental protocol is easy to implement, and the analytical model can be extended to a large variety of materials. The ability to characterize the time-dependence of the mechanical response of different materials at the nanoscale will enable a better estimation of the effect of manufacturing processes on the properties and performance of nanomaterials.

1. Introduction

The last decade has witnessed a rapid growth of nanotechnology advances and applications, creating an increasing need to identify and understand the mechanical behavior of different types of materials at the nanoscale. The mechanical properties of soft creeping materials such as metals,[1,2] polymers, [3-5] and biological materials [6] have been a common topic of research, aiming to understand their behavior under loads and deformations on the order of ~200 nm. Studies at these dimensions have brought to light phenomena, such as size dependence, directly related to the deformation response at these scales. Several studies have performed micro and nanomechanical tests using metallic and ceramic micropillars under compressive loads,[7,8] nanoindentation of metals and polymers,[2,9] and tension/torsion tests on nanowires. [10,11] The mechanisms underlying the mechanical behavior of these materials at the nanoscale have been directly attributed to the atomic and molecular arrangements of their crystalline or amorphous structures. For instance, crystalline materials exhibit plastic deformation dependent not only on the stress but also on the deformation gradient and material dimensions, where for dimensions lower than 10 μm the size dependence becomes pronounced, increasing the strain hardening.[11] Therefore, as the dimensions are reduced, the strength increases, as seen in metals and ceramics where the hardness increases with reduction of the indentation size.[12] Similarly, the deformation of amorphous polymers occurs by rotation and stretching of polymeric chains, leading to the dependence of their plastic mechanical response on the deformation rates.[13] Irrespective of the crystalline or amorphous nature of the material, its mechanical behavior at the nanoscale depends on different factors intrinsic to the specific material under study.[14,15] Thus, it is necessary to measure the deformation response at the nanoscale to understand the specific governing phenomena.

Modern nanofabrication techniques often require deforming materials at strain rates varying according to the fabrication process and its spatial resolution.[16] As an example, direct impression by laser fusion, used to nanopattern semiconductors and metals,[17] uses low strain rates ($\sim\dot{\varepsilon} \approx 10^{-4}\ s^{-1}$); hot embossing, often used to nanopattern polymers, uses medium strain rates ($\sim\dot{\varepsilon} \approx 10^{1}\ s^{-1}$); laser shock imprinting, used to nanoform metals, uses strain rates as high as $\dot{\varepsilon} \approx 10^{7}\ s^{-1}$. [18,19] Unfortunately, even though understanding the mechanical behavior of materials under these nanomanufacturing processes is

* Corresponding author.
E-mail addresses: jmunerao@eafit.edu.co (J.C. Múnera), dgoswami@purdue.edu (D. Goswami), rmartinez@purdue.edu (R.V. Martinez), eossa@eafit.edu.co (E.A. Ossa).

https://doi.org/10.1016/j.mechmat.2020.103443
Received 3 February 2020; Received in revised form 6 April 2020; Accepted 15 April 2020
Available online 23 May 2020

critical for their optimization, there is no appropriate methodology capable of measuring and predicting the strain rate dependence of the mechanical response of the processed materials at the nanoscale.

Soft materials under load exhibit an initially elastic response followed by a viscous, time-dependent behavior.[20,21] The time-dependence of the deformation behavior of soft materials at the nanoscale can be characterized by their indentation response at different penetration rates using an indenter with known geometry.[22,23] Following this approach here, we provide a tool to quantify the deformation response of time-dependent materials at depths lower than 20 nm. Previous studies have used the Hertz contact model to measure Young's modulus for materials with different stiffnesses. The measurement of a wide range of moduli has been usually performed for indentation depths between 2.5 and 12 nm using spherical tips with radius between $10 < R < 45$ nm, considering that the Hertz model is valid for depths $h < 0.4R$.[24-27] On the other hand, for viscoelastic materials, some studies have modeled their time-dependent behavior by using apparent stiffness modulus (E^*), analogous to spring responses to describe its elastic behavior, and dashpots to describe its viscous response.[28-30] Even though these analyses allow measurement and prediction of time-dependent material properties, they are based on finding functions relating loads and indentation depths at a given time by solving complex hereditary integrals, [6,30] which require substantial time and computational power. Additionally, simple two- or three -parameter models (such as Maxwell or Voigt) are often not precise enough to completely describe the time-dependent behavior of a material, forcing the addition of more parameters to the model, thus increasing the complexity of extracting model parameters from experimental results.

In order to fully understand the mechanical response of different time-dependent materials at the nanoscale, we report an experimental study of the indentation response of three materials with different nature and mechanical properties. One metal (Pb) and two polymers—poly(methyl methacrylate) (PMMA) and polystyrene (PS)—were indented at the sub-20 nm scale using commercial atomic force microscopy (AFM) probes. We also provide a nanoindentation model to analyze and predict the elastic and viscous (time-dependent) response of the materials. We demonstrate that this experimental methodology and the proposed analytical model can be used as a simple and reliable tool to study and predict the time-dependent mechanical behavior of nanomaterials independent of their nature.

2. Spherical indentation of creeping solids

Several classical models have been proposed to measure the stress and strain fields produced by a creeping solid under a rigid indenter (Fig. 1).[31-33] Bower et al. [32] solved the problem of axisymmetric indentation of a half-space formed by a creeping solid following a power law as:

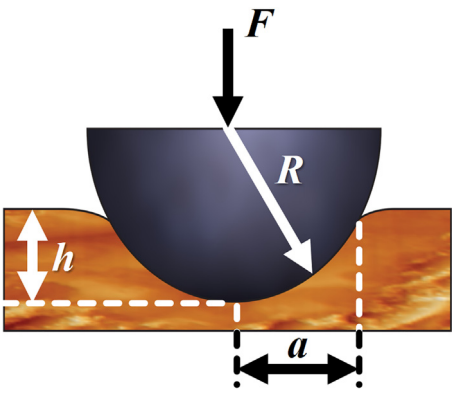

Fig. 1. Spherical indentation model of a half-space formed by a creeping solid.

$$\dot{\varepsilon} = \dot{\varepsilon}_0 \left(\frac{\sigma}{\sigma_0}\right)^n, \tag{1}$$

by using the similarity transformation suggested by Hill et al.[34], where σ_0 and $\dot{\varepsilon}_0$ are reference stress and reference strain rate respectively, and n is the power-law creep exponent of the material. We previously found that the reference stress can be approximated to $\sigma_0 \approx 0.1E$, where E is the Young's modulus of the material.[35,36] These transformations are based on the observation that at any given time, the velocity, stress and strain rate fields in the half-space only depend on the contact radius a and the penetration rate $\dot{h}$, and are independent of the load history for $h < 0.8R$ (Fig. 1). Thus, the general indentation problem is reduced to calculating stresses and displacements in a non-linear elastic solid, indented unit depth by a flat rigid indenter with unit radius (in the axisymmetric problem). In the case of indentation by a frictionless spherical indenter, the similarity solutions establish that the contact radius a relates to the indentation depth h, as [32]:

$$a = c\sqrt{2Rh}, \tag{2}$$

where R is the indenter radius. The constant c is a function of the material constant n and can be understood as the ratio between the real and nominal contact radii, where the nominal contact radius is $\sqrt{2Rh}$. Similarly, the applied load F^v is related to the indentation rate $\dot{h}$ *via* [32]:

$$\frac{F^v}{\pi a^2 \sigma_0} = \alpha\left(\frac{\dot{h}}{a\dot{\varepsilon}_0}\right)^{1/n} = \alpha\left(\frac{\dot{a}}{c^2\dot{\varepsilon}_0 R}\right)^{1/n}, \tag{3}$$

where the constant α is again a function only of the power-law exponent n. Values of c and α for selected values of n were deduced by Bower et al. [32] by a series of finite element analyses and are listed in Table 1. Equations (2) and (3) can be written in terms of effective stresses and strains below the indenter. The effective stress σ under the indenter is defined as:

$$\sigma = \frac{F}{\pi a^2}, \tag{4}$$

while the effective strain and strain rate under the indenter are specified as [32]:

$$\varepsilon = c\sqrt{\frac{h}{2R}}, \tag{5}$$

and

$$\dot{\varepsilon} = \frac{\dot{a}}{2R} = \frac{c\dot{h}}{2\sqrt{2hR}}, \tag{6}$$

respectively. Substitution of these definitions in Equations (2) and (3) give the empirical results from Mulhearn and Tabor [31]:

$$\dot{\varepsilon} = \left(\frac{\sigma}{\alpha\sigma_0}\right)^n \frac{\dot{\varepsilon}_0 c^2}{2}, \tag{7}$$

for the strain rate under an indenter in a power-law creeping solid.

3. Materials and Methods

3.1. Materials

Materials with different nature and mechanical properties, but with known time-dependent mechanical responses, were selected in the experimental part of this study to validate the findings under a wide variety of conditions. Three different materials known to show a time-dependent creeping response were selected to study their mechanical behavior at the nanoscale: a low melting point metal (Pb) and two thermoplastic polymers, PMMA and PS.

Thin films of PMMA and PS with thicknesses between 400 nm and

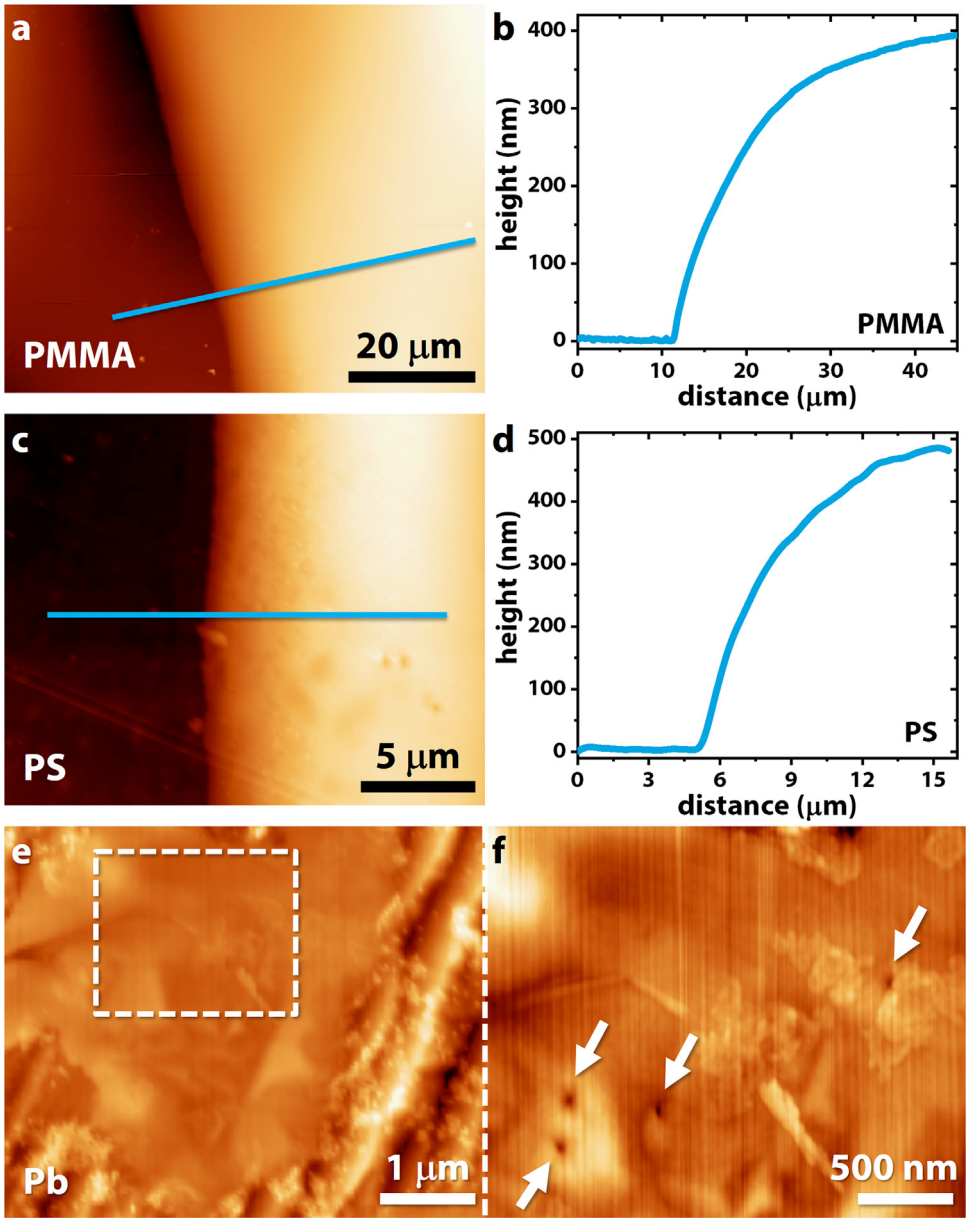

Fig. 2. Representative samples used in this study. (a) AFM topography image of a spin-coated PMMA nanolayer. (b) AFM cross-section showing the profile of the PMMA sample in (a). (c) AFM topography image of a spin-coated PS nanolayer. (d) AFM cross-section showing the profile of the PS sample in (c). (e, f) Representative Pb sample surface (e) before and (f) after several indentations (shown by white arrows).

500 nm (see Fig. 2a–d) were produced by dissolving pellets in concentrations of 5% in weight in Xylene and γ-Valerolactone, respectively (both reagents in purity grades ≥ 98.5%). Approximately 100 μL of solution was placed on glass substrates, previously cleaned by ultrasonic immersions of acetone, IPA and deionized water for 2 minutes each. A spin-coating process with an angular speed of 3500 rpm for 45 s was used to obtain thin films free of impurities.

Lead was selected as several works have used this metal (both pure and alloyed) to study its time-dependent properties by indentation.[37-40] Pb samples were prepared by melting ~200 g of the pure metal in a graphite crucible at a temperature of 673 K in a furnace. The material was kept at that temperature for ~30 min, which is sufficient to form a uniform fluid. A small amount of the melted material (~20 g) was then poured on a stainless-steel disc of 15 mm diameter, previously heated for 15 min at 573 K to avoid any thermal shock that may affect the microstructure of the material. The samples were then cooled down to room temperature until their complete solidification, thus creating smooth, flat surfaces appropriate for AFM analysis (see Figs. 2e-f). These samples were kept in a sealed container at room temperature for at least 24 hours prior to testing. Special care was taken in order to avoid oxide formation on the surface of the samples that might affect the measurements.

The surface morphology is an important condition to consider when nanoscale properties must be obtained. To acquire reliable results, we estimate that the surface roughness of the tested material must be $Ra \leq 0.01R$, allowing 1% error in the measurements. It is worth mentioning that in our measurements we had an average $Ra = 0.12$ nm ($Ra = 0.005R$) on a 1μm x 1μm measuring window in the materials tested.

3.2. AFM calibration

Appropriate calibration of the AFM measurements is important to have an adequate analysis of the measured properties.[41] Calibration

refers to the protocols required to adjust values measured by a piece of equipment by comparing it to reference external values. The calibration of the AFM equipment in this study involved the following variables: sensitivity, contact force, reference stiffness, and indentation rate.

3.2.1. Sensitivity calibration

Cantilever sensitivity calibration was performed by approaching the tip of the AFM probe to a sample material considered several orders of magnitude stiffer than the tip. As the sample is stiffer than the tip, it is possible to directly relate all the signals obtained by the AFM photodiode to the cantilever deflection, neglecting any sample deformation. In this study, we used a flat and polished SiC sample to perform the sensitivity calibrations. The sensitivity can be obtained from an *F–Z* response as the inverse of the slope of the approach region.[19] The sensitivity of the cantilever was measured after each test to detect any possible change in the measurements.

3.2.2. Cantilever stiffness calibration

Sader's method[42] was followed in this study to obtain the cantilever stiffness k as:

$$k = 0.19061 L Q \omega_r^2 b^2 \rho \Gamma_I(\omega_r) \tag{8}$$

where, Q is the quality factor of the first harmonic of the cantilever, which can be measured by dividing the resonant frequency (ω_r) by its bandwidth ($\Delta\omega$); b is the cantilever width and L its length. ρ represents the density of the fluid where the cantilever is vibrating. $\Gamma_I(\omega_r)$ is the imaginary part of the hydrodynamic function of the system. This last variable depends on the Reynolds number of the cantilever in the fluid as a function of the square of the cantilever width, frequency, density, and fluid viscosity. To find k, the vibrational and geometric characteristics of the cantilever must be measured. The dimensional characteristics of the cantilevers were measured by SEM, while the vibrational characteristics were measured by the natural frequency of the cantilever-tip system.

3.2.3. Penetration rate

In an AFM, it is only possible to control the piezo speed, i.e. the approach rate of the cantilever to the sample. However, the penetration rate of the tip into the sample depends on the properties of the particular sample. To measure the indentation rate, it is necessary to record the variation of penetration (h) with the test time. Fig. 3 shows the penetration rate response for a given piezo speed of 500 nm/s, where the indentation rate reaches an approximately constant value of 166 nm/s after approximately 30 ms. The response of the penetration rate

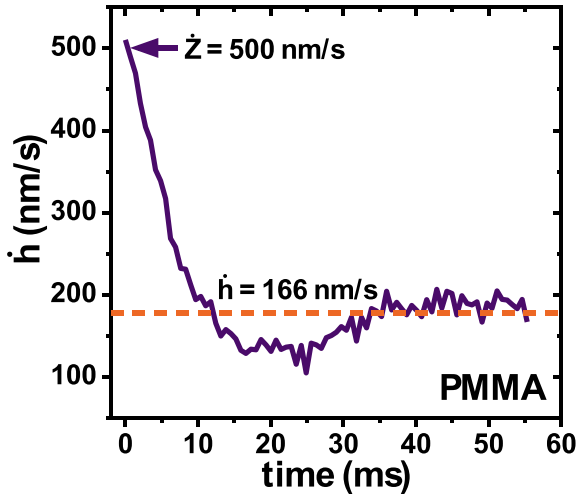

Fig. 3. Measured indentation rate for a selected controlled piezo speed of 500 nm/s on PMMA.

was analyzed for each test to find the appropriate value of the indentation rate employed. Further, this methodology allowed us to exclude from the analysis any test with variable values of penetration rate.

3.3. Nanoindentation tests

Nanoindentation tests were performed at standard conditions (T = 293 K and R.H. = 50%) using an atomic force microscope (AFM; XE7, Park Systems Inc.). Commercial silicon AFM tips with diamond-like carbon (DLC) coating (TAP150, Budget Sensors) having a nominal stiffness k = 5 N/m and tip radius R = 25 nm (Fig. 4) were used to obtain the force curves. The AFM tips were imaged before and after indentations to verify that they do not suffer significant changes in radius. We performed indentations in different regions of the tested materials at 8 piezo speeds varying from 10 to 1300 nm/s; each measurement was repeated 10 times. We recorded load (F), piezo displacements (Z), and time during each indentation. The experimental results were evaluated using a statistical hypothesis test consisting of an analysis of median differences with a significance level of 5%, aiming to establish statistically acceptable differences. Note that the main interest of this work was to describe the response of the materials during the penetration of the tip, thus the retraction information was not considered here.

4. Results

Fig. 5a–c shows the dependence on the piezo displacement (Z) of the applied force (F) in Pb, PMMA and PS for five different piezo speeds ($\dot{Z}$). The slopes of these graphs correspond to the contact stiffness (S), which increases with increasing piezo speeds (Fig. 5d). The strong linear correlation (R^2_{Pb} = 0.968; R^2_{PMMA} = 0.989; R^2_{PS} = 0.936) between S and $\dot{Z}$ indicates the time-dependent behavior of these materials. To ensure that this time-dependence of S is caused by the mechanical response of the material and not due to any instrumental artifact, we also tested a stiff elastic material (SiC) and found no time-dependent effects on its deformation, as shown by the horizontal line in Fig. 5d (R^2_{SiC} = 0.976).

Fig. 6a–c shows the dependence between F and the actual penetration depth (h), which is obtained by subtracting the cantilever deflection from the piezo displacement, $h = Z - \delta$. The initial material response ($h \leq 2$ nm) shows an apparent elastic behavior according to the Hertz contact model,[43] not significantly dependent on the indentation rate, $\dot{h} = \Delta h/\Delta t$. After the initial elastic deformation ($h \geq 2$ nm), an inflection in the indentation response appears, exhibiting a strong dependence on the indentation rate. Since the elastic response is independent of the indentation rate and only depends on the atomic bond stiffness,[11] the deformation behavior upon an applied force (F) can be considered as the sum of its elastic (F^e) and viscous (F^v, time-dependent) components ($F = F^e + F^v$; also see Fig. 9d–f).

An analysis of the effect of $\dot{h}$ on F during tip penetration shows that, for a constant arbitrary depth (e.g., h = 6.5 nm), the mechanical response follows a power law as (Fig. 6d–f):

$$\dot{h} = \dot{h}_0 \left(\frac{F}{F_0}\right)^{n_0}, \tag{9}$$

where $\dot{h}_0$ is a reference indentation rate, F_0 is a reference applied force, and n_0 is the power-law exponent describing each material (see Table 2).

The indentation tests performed revealed that the power-law relation described above can be viewed as the relation between load and indentation rate for a given indentation depth. Analysis of this power-law response for different indentation depths revealed that the power-law exponent n_0 remains constant independent of the depth reached by the indenter, as shown in Fig. 6d-f for the different materials tested.

This material response can in turn be described by a power-law creeping behavior, such as Bower's model,[32] which gives the steady-

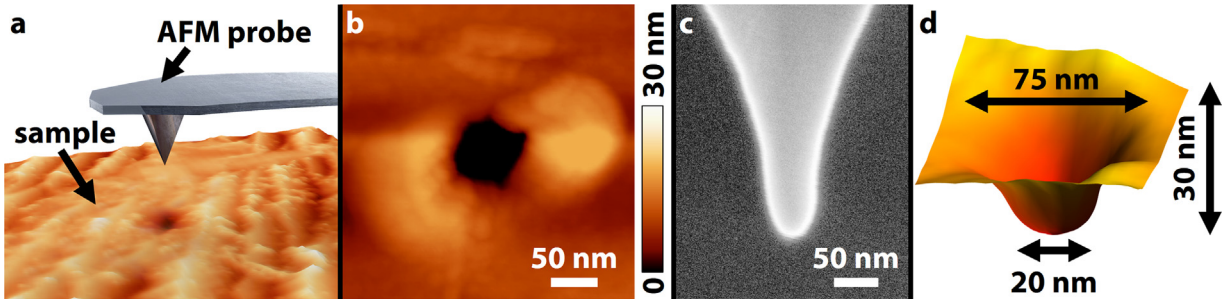

Fig. 4. AFM nanoindentation test. (a) Schematic diagram of the AFM nanoindentation system. (b) Topographical image of a representative indentation on PMMA. (c) SEM image of the spherical tip of a representative commercial AFM probe used for the nanoindentation. (d) 3D AFM topographical image showing the geometry of the nanoindentation in (b).

state time-dependent response of the material as shown in Equation (1).

Fig. 7 shows the experimental dependence of $\dot{\varepsilon}$ on σ for two constant selected ε (e.g., 0.1 and 0.2). These results can also be described by Bower's power law formulation (Equation 7) with the parameters listed in Table 3. Note that for the different strains analyzed, the power-law exponent n remains constant, as shown in Fig. 7a-c for the different materials tested. We previously demonstrated that $\dot{\varepsilon}_0$ for creeping solids can be considered as a strain-dependent parameter, [36] irrespective of the strain history of the material. Thus, it is expected that Bower's formulation can be extended to give the relation between the stress and strain rate at any value of strain ε by replacing the constant $\dot{\varepsilon}_0$ with a reference strain rate $\dot{\varepsilon}_0(\varepsilon)$ that is a function of strain ε. Thus Equation (7) can be rewritten to obtain $\dot{\varepsilon}_0(\varepsilon)$ as:

$$\dot{\varepsilon}_0(\varepsilon) = \frac{h}{2cR\varepsilon}\left(\frac{\alpha\sigma_0}{\sigma}\right)^n. \tag{10}$$

To test this hypothesis, we evaluate $\dot{\varepsilon}_0$ as a function of ε at the nanoscale. The indentation results were used as follows: From each experimental F–h curve, $\dot{\varepsilon}_0$ is obtained from Equation (10), where σ is calculated from Equation (4) and ε is calculated using Equation (5), for $\varepsilon \geq 0.05$. At $\varepsilon = 0$, $\dot{\varepsilon}_0 = \infty$, since $\sigma = 0$. Therefore, $\dot{\varepsilon}_0$ must be estimated for $\varepsilon > 0$. The time-dependent behavior defined by Equation (7) is not expected to be precise at small strains, since the elastic (time-independent) component of the material dominates the strain response. This procedure was repeated across a range of ε values to obtain calibration curves $\dot{\varepsilon}_0(\varepsilon)$. Since these curves overlap, within experimental error, for different $\dot{h}$ (see Fig. 8), the average of these curves can be used as a master curve to predict the mechanical behavior of the materials in the studied range of ε, demonstrating the validity of the extension (Equation 10) to Bower's model. This approach is similar to some metal plasticity theories where the yield strength is taken to be strain-dependent. Physically this can be rationalized by recalling that the molecular chains in polymers rearrange with deformation, just as the yield strength of metals is a function of accumulated plastic strain due to the evolution of the dislocation structure.

5. Analytical model

We now propose an analytical model capable of predicting the mechanical behavior under applied force based on the experimental material response for time-dependent materials at the nanoscale. The model is derived based on the following assumptions: (*i*) the indentation response at the nanoscale using commercial AFM probes can be approximated to spherical indentations up to maximum depths of $a/D = 0.4$ (Fig. 1), reaching maximum effective strains $\varepsilon \approx 0.4$; (*ii*) physical phenomena present near the surface (friction, adhesive, attractive, and repulsive forces) are neglected, as the forces causing the deformation of the material are considerably greater than these; (*iii*) the Hertz contact model[44] can accurately describe the elastic response of the materials, with a Young's modulus independent of $\dot{\varepsilon}$; (*iv*) the viscous (time-dependent) response of the material at a constant temperature is appropriately described by a power-law model following Bower's formulation,[32] with $\dot{\varepsilon}_0(\varepsilon)$ as described by Ossa et al.[35]; and (*v*) the changes in S reflect the actual material deformation after $\dot{Z}$ correction (Fig. 3).

The total effective stress σ on the material is then written as the sum of its elastic σ^e and viscous (time-dependent) σ^v components. Thus, for a given arbitrary load history, σ can be written as:

$$\sigma = \sigma^e + \sigma^v, \tag{11}$$

with the elastic response given by:

$$\sigma^e = \frac{8\pi}{3\sqrt{2}}\left(\frac{E}{1-\nu^2}\right)\varepsilon, \tag{12}$$

where, E is the Young's modulus and ν the Poisson's ratio of the material. The viscous response of the material can be written as:

$$\sigma^v = \alpha\sigma_0\left(\frac{2\dot{\varepsilon}}{c^2\dot{\varepsilon}_0(\varepsilon)}\right)^{1/n}. \tag{13}$$

To obtain the stress produced by a given strain history it is necessary to solve Equations (11)–(13) for a given time.

Fig. 9 demonstrates the accuracy of the proposed analytical model

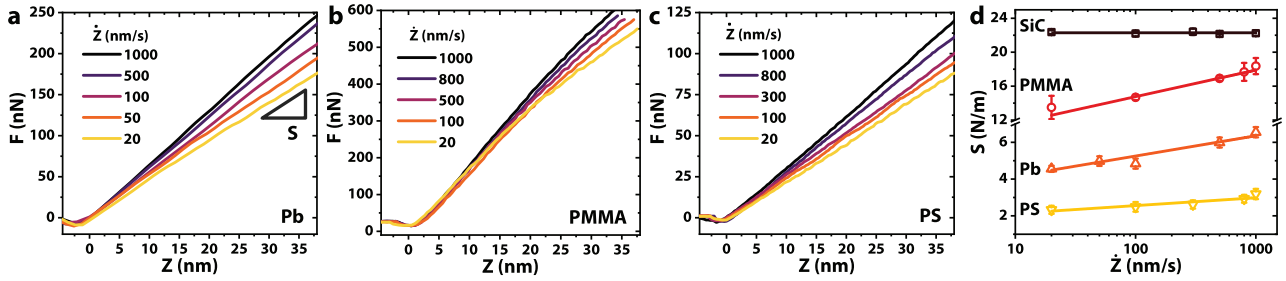

Fig. 5. Time-dependent nanomechanical response of Pb, PMMA, and PS up to a piezo displacement (Z) of 40 nm after contact. (a–c) F–Z curves for Pb, PMMA, and PS, respectively, at five different piezo speeds ($\dot{Z}$). (d) Comparison between the contact stiffness (S) of time-dependent materials (Pb, PMMA, PS) and a non-time-dependent material (SiC), as a function of $\dot{Z}$.

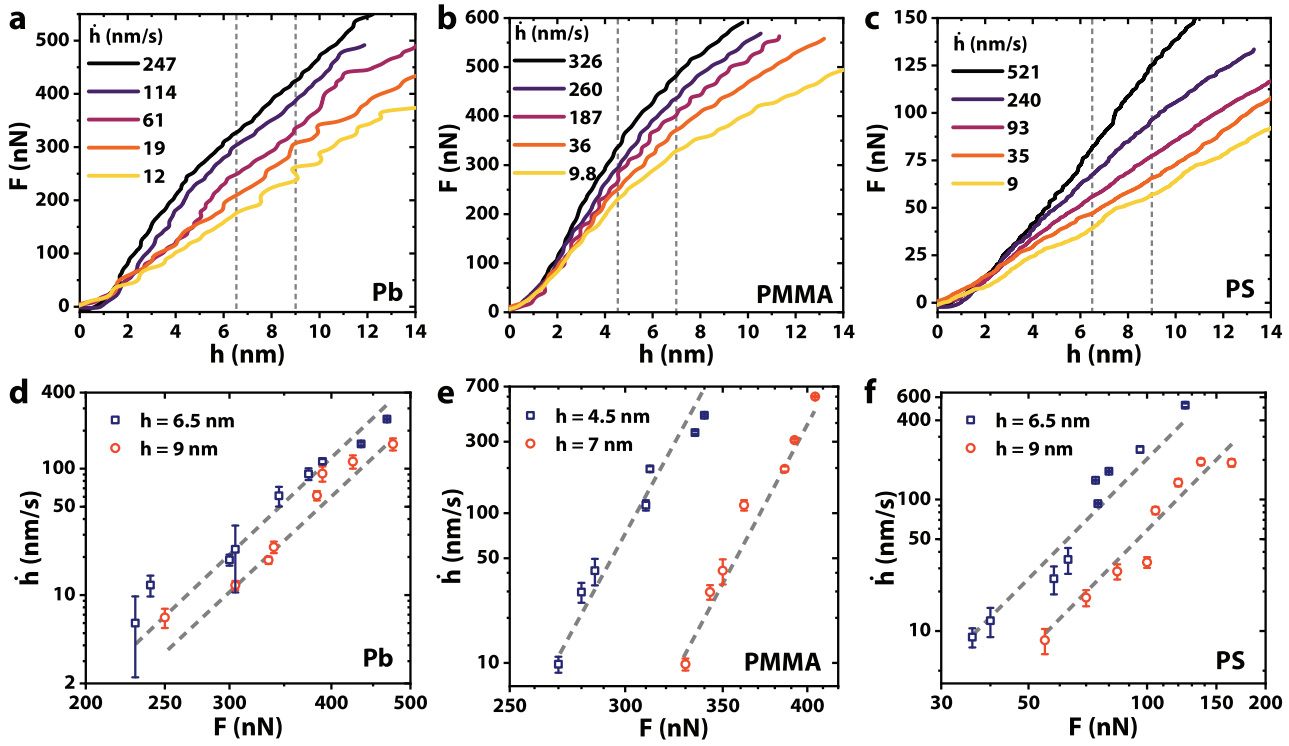

Fig. 6. Dependence on the penetration depth (h) of the applied Force (F) for (a) Pb, (b) PMMA, and (c) PS at different indentation rates ($\dot{h}$). (d–f) Log-log plots of $\dot{h}$–F response for Pb, PMMA, and PS, respectively, at two different penetration depths, showing that the slope is independent of h for the same material. Hollow circles and squares represent experimental results ($N = 10$), while dashed lines represent model predictions (Equation 9).

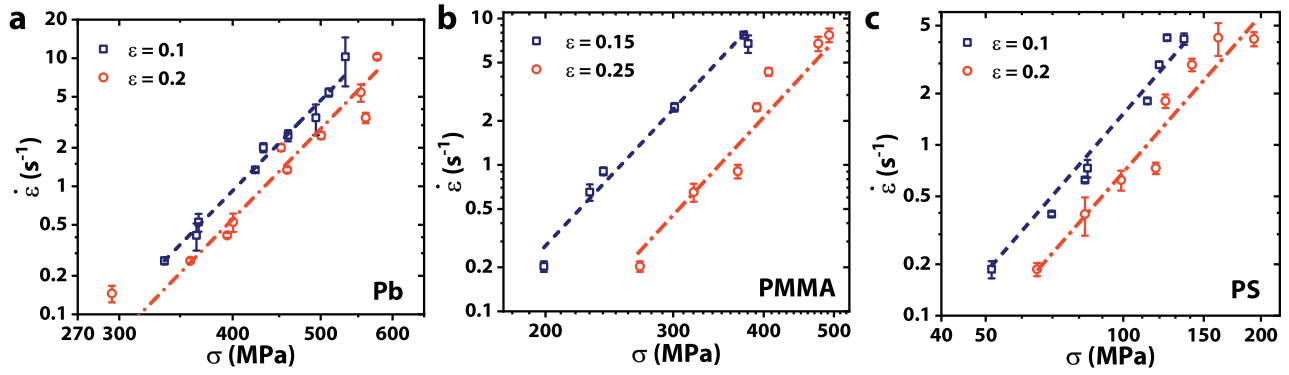

Fig. 7. Dependence on the effective stress of the effective strain rate for (a) Pb, (b) PMMA, and (c) PS. Hollow circles and squares represent experimental results ($N = 10$), while dashed lines represent model predictions (Equation 7; log-log plot). The slope is independent of ε for the same material.

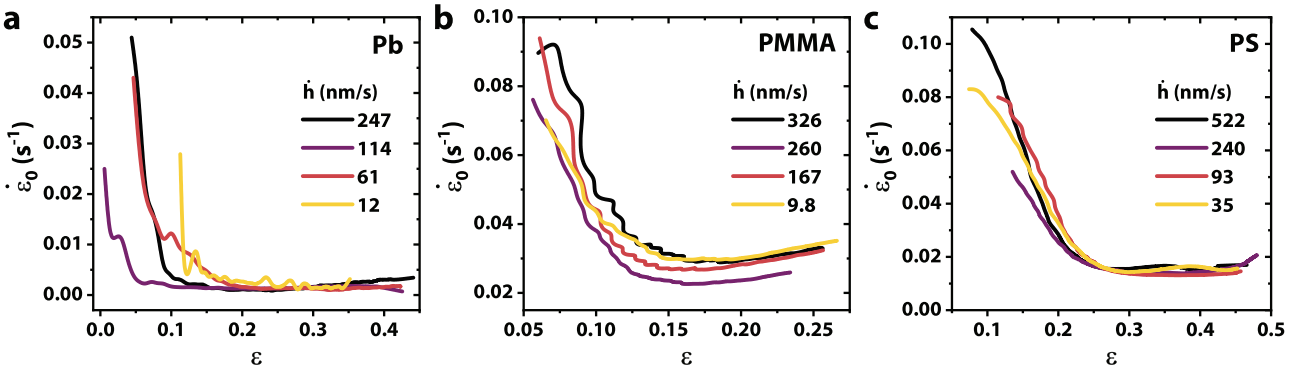

Fig. 8. Calibration curves $\dot{\varepsilon}_0(\varepsilon)$ for (a) Pb, (b) PMMA, and (c) PS at different penetration rates ($\dot{h}$). The overlapping of these curves for a particular material demonstrates their independence of the penetration rate.

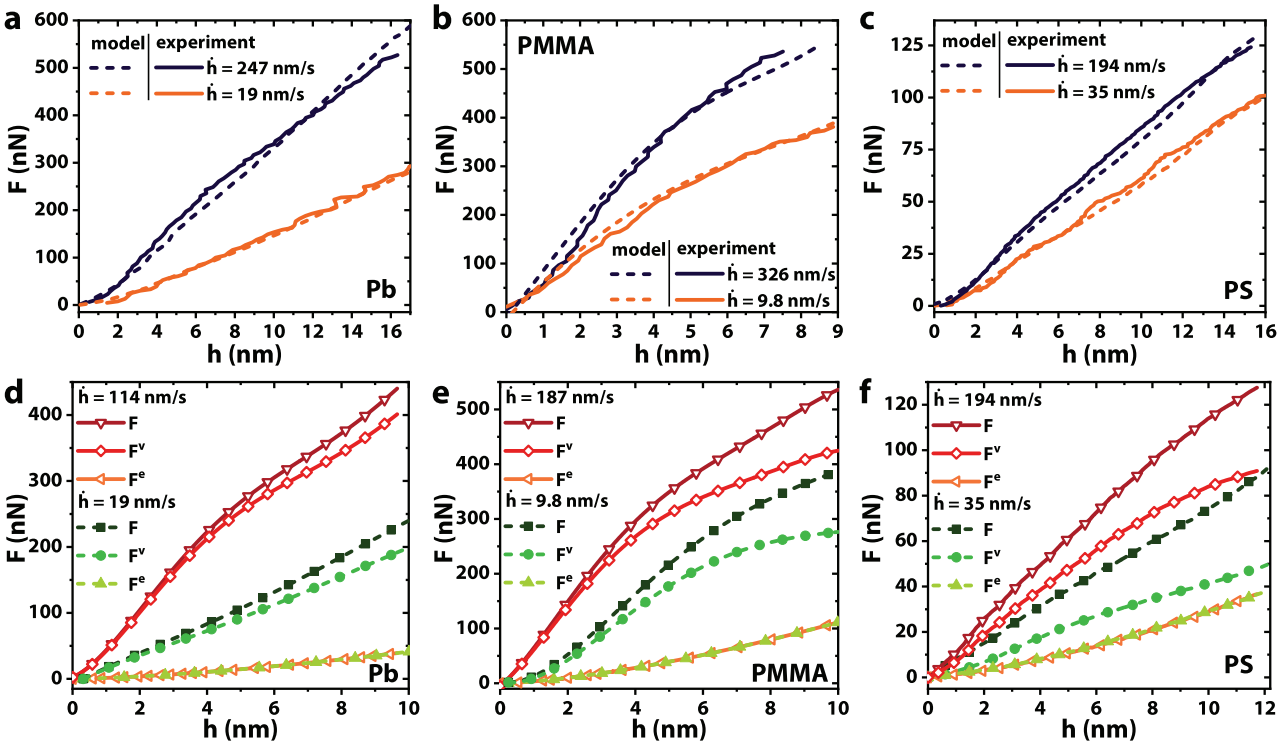

Fig. 9. Comparison between the experimental results and the proposed analytical model predicting the *F*–*h* mechanical response at different penetration rates for (a) Pb, (b) PMMA, and (c) PS. Model prediction of the applied force (*F*) as the sum of its elastic (F^e) and viscous (F^v) components for (d) Pb, (e) PMMA, and (f) PS.

to predict the *F*–*h* response at different $\dot{h}$ (material parameters listed in Table 3). Note that we used different experimental results to obtain the calibration function $\dot{\varepsilon}_0(\varepsilon)$ (Fig. 8) than those used to demonstrate the accuracy of our model (Fig. 9). Fig. 9d-f show the independent elastic and viscous responses, demonstrating how, following a Maxwell description (Equation 11), where the elastic and viscous components work in series, it is possible to accurately capture the overall response of the material, leading to good agreements with experimental results.

Fig. 10 shows the stress–strain response for selected indentation tests on the materials studied following the model proposed, showing good agreement between experiments and model.

6. Approximate calibration of the model

Four parameters, *E*, *n*, $\dot{\varepsilon}_0(\varepsilon)$, and σ_0 characterize the deformation behavior in the model proposed to describe the mechanical behavior under load in a time-dependent material at the nanoscale. An approximate calibration procedure with three steps, requiring a minimum of two nanoindentation tests is described below:

Step 1: The first step is related to the characterization of the time-dependent (viscous) behavior. Two indentation tests at different piezo speeds $\dot{Z}_1 \neq \dot{Z}_2$ (e.g. $\dot{Z}_1 = 10$ nm/s and $\dot{Z}_2 = 1000$ nm/s) must be performed. For each of the tests the penetration rates $\dot{h}$ must be measured, and for a given indentation depth $h_0 > h_e$ (e.g. $h_0 = 12$nm with $h_0 < 0.4D$) its respective measured values of load F_1 and F_2 must be found. Then, Equation (9) can be used to get:

$$n_0 = \frac{\log(\dot{h}_1/\dot{h}_2)}{\log(F_1/F_2)}, \tag{14}$$

α and c can be found in Table 1. Now use Equations (4) and (6) to calculate σ and $\dot{\varepsilon}$ for each of the tests at the depth h_0 and then find n, using:

Table 1
Values for the parameters n, α, and c from the power- law model (reproduced from Bower et al. [32]).

n	α	c
1	0.849	0.707
1.11	1.085	0.747
1.25	1.332	0.788
1.43	1.602	0.831
1.66	1.886	0.875
2	2.176	0.92
2.5	2.465	0.966
3.33	2.734	1.013
5	2.973	1.065
10	3.11	1.128
100	3.051	1.201

Table 2
Estimated values from the power- law model in Equation (9).

Parameter	Pb	PMMA	PS
n_0	7.24	17.77	3.38
$\dot{h}_0$ (nm/s)	10.22	0.80	1.06
F_0 (nN)	281.23	433.03	31.36

Table 3
Indentation model parameters for the tested materials.

Parameter	Pb	PMMA	PS
n	6.14	15.60	3.15
α	1.27	1.32	1.12
c	0.82	0.65	0.82
σ_0 (MPa)	331	364	59
E (GPa)	3.31	3.64	0.59

$$n = \frac{\log(\dot{\varepsilon}_1/\dot{\varepsilon}_2)}{\log(\sigma_1/\sigma_2)}, \tag{15}$$

and calculate again the values of α and c for n.

Step 2: The second step constitutes characterizing the elastic behavior of the material: obtaining the Young's modulus, E. The two indentation results previously used can be employed to extract this parameter. The trajectories of both indentation responses can be expressed as:

$$\text{for } \dot{Z}_1 \rightarrow F_1 = F_1^e + F_1^v, \tag{16}$$

$$\text{for } \dot{Z}_2 \rightarrow F_2 = F_2^e + F_2^v, \tag{17}$$

where, F is the experimentally measured load. F^v is the load component corresponding to the time-dependent (viscous) response (Equation 3); while F^e represents the Hertzian elastic response during indentation: $F_e = 4E\sqrt{R}h^{3/2}/3(1-\nu^2)$. Substitution of (3) and F_e in (16) and (17) and replacing, gives:

$$E = \frac{F_2 - AF_1}{\frac{3\sqrt{R}}{4(1-\nu^2)}(h_2^{3/2} - Ah_1^{3/2})}, \tag{18}$$

where $A = (\frac{h_2}{h_1})(\frac{\dot{h}_2}{\dot{h}_1})^{1/n}$. In this solution, we assumed, from experience and previous results, that the reference stress can be approximated as $\sigma_0 \approx 0.1E$ and the value of Poisson's ratio ν was known for the material tested.

Step 3: Finally, the calibration function $\dot{\varepsilon}_0$ can be found from one of the experimental results as:

$$\dot{\varepsilon}_0(\varepsilon) = \frac{\dot{h}}{a}\left(\frac{\alpha\pi a^2\sigma_0}{F^v}\right)^n, \tag{19}$$

where, a is found from Equation (2) and F^v is calculated as:

$$F^v = F - F^e \tag{20}$$

Thus, a minimum of two indentation tests at different piezo speeds suffice to approximately calibrate the proposed model. A higher number of tests can be performed to increase the statistical accuracy of the fitted parameters and hence ensuring the uniqueness of the results.

The unique determination of mechanical properties from instrumented indentation methods has been a subject of recent study, leading to the use of neural network methods to improve the accuracy from experimental results on inverse problems. Recently, Lu et al.[45] exploited the capabilities of deep-learning algorithms to ensure the uniqueness of the mechanical behavior of results obtained from instrumented indentation. It is expected that the implementation of such technologies along with the experimental methodologies described in this work would improve the accuracy of the results obtained. This work is proposed as a topic which merits future study.

7. Discussion

A simple methodology to extract time-dependent properties of materials at the nanoscale consisting of AFM indentation tests has been developed. By testing three very dissimilar materials we intended to evaluate any possible limitation to capture the time-dependent behavior at the nanoscale. However, our model proved to be able to capture the response even with these differences in material nature.

It is worth considering that our model was based on the solution of the problem of axisymmetric indentation of a half-space formed by a creeping solid. The half-space condition can be reached if the sample thickness tested is at least $t \geq 5h$. The proposed model is able to describe the material behavior for indentation depths lower than 20 nm using a tip diameter $D = 50$ nm and a minimum of 2 indentation tests. This model was evaluated for $10^{-1} < \dot{\varepsilon} < 10^{1}\ s^{-1}$, reaching piezo speeds ranging $10 < \dot{Z} < 1300$ nm/s. If the material response at higher values of $\dot{\varepsilon}$ is required, $\dot{Z}$ must be increased. However, for $\dot{Z} > 1500$ nm/s, the impact forces during the initial tip-sample contact must be considered. On the other hand, for $\dot{Z} < 10$ nm/s, we suggest using a load-controlled indentation instead of the piezo speed control.[46] We expect the material response to be independent of the control method used for the indentation.

Since the experimental F–Z curves of the tested materials exhibit minimal adhesive tip-sample effects (negligible negative forces in Fig. 5a–c), our initial assumption of frictionless contact is valid. Recalling that the self-similar analysis of Bower et al. [32], and the determination of the constants c and α for frictionless conditions are valid for $a/D < 0.4$, our experiments were valid up to maximum indentation depths of $h_{Pb} = 11.9nm$, $h_{PMMA} = 18.9nm$ and $h_{PS} = 11.9nm$. Beyond these indentation depth levels, finite strain effects play a significant role and the simple model presented here is expected to be unable to capture the indentation response. Full finite element solutions of the field equations would be necessary to obtain the indentation response in such cases. On the other hand, if the adhesive forces are high, the model can be easily adjusted to extract properties with tip-sample friction by replacing the parameters α and c from Table 1 with the parameters obtained by Bower et al. [32] for adhesive friction contact. However, special care must be taken under such conditions as the determination of the constants c and α are valid only for $a/D < 0.2$.

The F-h responses during nanoindentation predicted by the proposed model show that the elastic behavior of the time-dependent

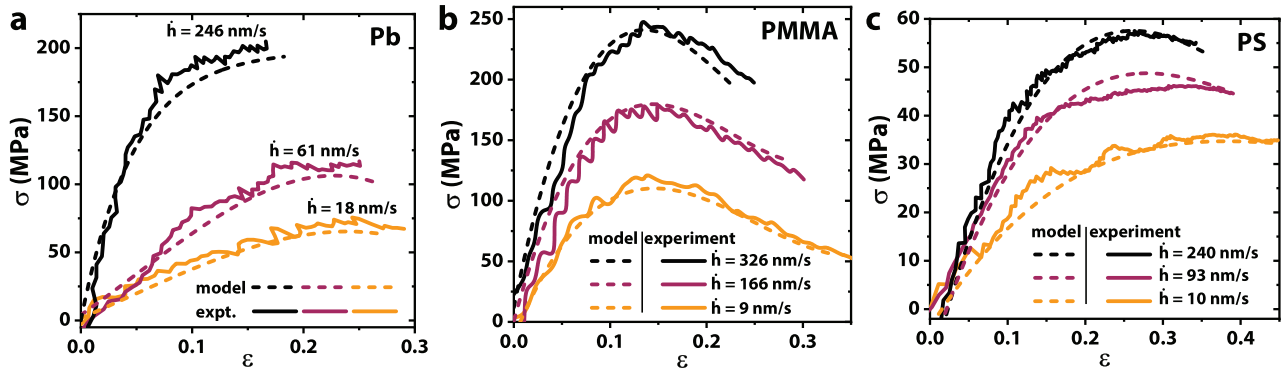

Fig. 10. Comparison between the experimental results and the proposed analytical model predicting the $\sigma - \varepsilon$ response at different penetration rates for (a) Pb, (b) PMMA, and (c) PS.

materials studied can be characterized by an elastic (time-independent) component, which is independent of the loading rate, and a viscous component fully dependent on loading rate. Fig. 9d-f shows that the elastic components of the three materials studied can be considered fully independent on the loading rate, in contrast to other models that propose the use of elastic rate-dependent components (E^*).[28-30]

The $\sigma - \varepsilon$ responses shown in Fig. 10 start with a quasi-linear behavior [47] followed by a nonlinear regime with different responses for the three materials studied. Pb exhibits an initial linear behavior followed by quasi-intermittent deformation packages (bursts) without apparent strain hardening (Fig. 10a). For metals, the strain response at nanometric levels is governed mainly by strain packages induced once a necessary energy has been reached to begin the movement of the dislocation density existing in the volume of the contact region.[48,49] PMMA, on the other hand, shows a pronounced drop in stresses after $\varepsilon \approx 0.15$ (Fig. 10b), indicating a strain-softening process. [50] PS shows an approximately constant stress behavior for $\dot{h} < 93$ nm/s (Fig. 10c), implying that the material has reached a fully plastic flow. [51] In the case of polymers, the nanoscale deformation mechanisms can be explained by softening due to free volumes or flexure of the polymeric chains.[52-54] A unified theory explaining the deformation mechanisms at the nanoscale, however, has not yet been established and further work in this area is required.

It is important to note that the mechanical properties of thermoplastic polymers and soft metals are not only strongly dependent on time, as described in this paper, but also on temperature.[55] The model proposed here can be easily extended to incorporate temperature effects on the mechanical behavior, following well-established temperature models.[56,57] For instance, it has been proven that for crystalline solids the energy-activated Arrhenius equation is useful to describe the effect of temperature on the time-dependent properties. [58] In the case of polymers, temperature effects are usually described by the Williams-Landel-Ferry equation,[57] which employs a superposition principle considering the intrinsic characteristics of the material (i.e., glass transition temperature, free volume, etc.).[59]

8. Concluding remarks

In summary, we proposed a simple methodology to characterize and analytically model the mechanical properties of time-dependent materials at the nanoscale. This methodology can be implemented on any AFM system using commercially available probes. Our proposed model describes the material's behavior as the sum of its elastic (Hertz contact model) and time-dependent components (power-law model). This analytical model requires only two sub-20 nm *F–Z* curves (at different piezo speeds) to accurately describe the mechanical behavior of a tested material across strain rates ranging $10^{-1} < \dot{\varepsilon} < 10^{1}$ s^{-1}, which is relevant for common parallel nanopatterning processes such as nanoimprint or step-and-flash imprint lithography. Additionally, this model is independent of the stress history of the material since it uses a formulation in which one of its parameters ($\dot{\varepsilon}_0$) is a function of the material strain. We envision that the proposed methodology will enable the optimization of the outcomes of large-scale nanomanufacturing techniques in light of the nano-mechanical properties of the processed material.

CRediT authorship contribution statement

Juan Camilo Múnera: Investigation, Formal analysis, Writing - original draft. **Debkalpa Goswami:** Formal analysis, Visualization, Writing - review & editing. **Ramses V. Martinez:** Resources, Writing - review & editing. **E. Alex Ossa:** Conceptualization, Methodology, Resources, Supervision, Writing - review & editing.

Declaration of Competing Interests

None.

References

Dunaevskiy, M., Geydt, P., Lähderanta, E., Alekseev, P., Haggrén, T., Kakko, J.-P., Jiang, H., Lipsanen, H., 2017. Young's modulus of wurtzite and zinc blende inp nanowires. Nano Letters 17 (6), 3441–3446.

Sypien, A., Garzel, G., Czeppe, T., 2019. Thermomechanical behavior of amorphous alloys based on titanium at the temperature range of the glass transition and crystallization. Materials Science and Engineering: A 743, 77–86.

Chevalier, J., Brassart, L., Lani, F., Bailly, C., Pardoen, T., Morelle, X.P., 2018. Unveiling the nanoscale heterogeneity controlled deformation of thermosets. Journal of the Mechanics and Physics of Solids 121, 432–446.

Voyiadjis, G.Z., Malekmotiei, L., Samadi-Dooki, A., 2018. Indentation size effect in amorphous polymers based on shear transformation mediated plasticity. Polymer 137, 72–81.

Benaglia, S., Amo, C.A., Garcia, R., 2019. Fast, quantitative and high resolution mapping of viscoelastic properties with bimodal afm. Nanoscale 11, 15289–15297.

Garcia, P.D., Garcia, R., 2018. Determination of the viscoelastic properties of a single cell cultured on a rigid support by force microscopy. Nanoscale 10, 19799–19809.

Taloni, A., Vodret, M., Costantini, G., Zapperi, S., 2018. Size effects on the fracture of microscale and nanoscale materials. Nature Reviews Materials 3 (7), 211–224.

Greer, J., Oliver, W., Nix, W., 2006. Corrigendum to “size dependence in mechanical properties of gold at the micron scale in the absence of strain gradients. [acta mater 53 (6) (2005) 1821–1830]. Acta Materialia 54 (6), 1705.

Lam, D.C.C., Chong, A.C.M., 1999. Indentation model and strain gradient plasticity law for glassy polymers. Journal of Materials Research 14 (9), 3784–3788.

Weinberger, C.R., Cai, W., 2012. Plasticity of metal nanowires. J. Mater. Chem. 22, 3277–3292.

Fleck, N., Muller, G., Ashby, M., Hutchinson, J., 1994. Strain gradient plasticity: Theory and experiment. Acta Metallurgica et Materialia 42 (2), 475–487.

Nix, W.D., Gao, H., 1998. Indentation size effects in crystalline materials: A law for strain gradient plasticity. Journal of the Mechanics and Physics of Solids 46 (3), 411–425.

Fetters, L.J., Lohse, D.J., Richter, D., Witten, T.A., Zirkel, A., 1994. Connection between polymer molecular weight, density, chain dimensions, and melt viscoelastic properties. Macromolecules 27 (17), 4639–4647.

Zhu, T., Li, J., 2010. Ultra-strength materials. Progress in Materials Science 55 (7), 710–757.

Peng, C., Zhong, Y., Lu, Y., Narayanan, S., Zhu, T., Lou, J., 2013. Strain rate dependent mechanical properties in single crystal nickel nanowires. Applied Physics Letters 102 (8), 083102.

Ye, C., Liao, Y., Cheng, G.J., 2010. Warm laser shock peening driven nanostructures and their effects on fatigue performance in aluminum alloy 6160. Advanced Engineering Materials 12 (4), 291–297.

Vorobyev, A.Y., Guo, C., 2013. Direct femtosecond laser surface nano/microstructuring and its applications. Laser & Photonics Reviews 7 (3), 385–407.

Gao, H., Hu, Y., Xuan, Y., Li, J., Yang, Y., Martinez, R.V., Li, C., Luo, J., Qi, M., Cheng, G.J., 2014. Large-scale nanoshaping of ultrasmooth 3d crystalline metallic structures. Science 346 (6215), 1352–1356.

Goswami, D., Munera, J.C., Pal, A., Sadri, B., Scarpetti, C.L.P.G., Martinez, R.V., 2018. Roll-to-roll nanoforming of metals using laser-induced superplasticity. Nano Letters 18 (6), 3616–3622 PMID: 29775318.

Hu, Y., Xuan, Y., Wang, X., Deng, B., Saei, M., Jin, S., Irudayaraj, J., Cheng, G.J., 2016. Superplastic formation of metal nanostructure arrays with ultrafine gaps. Advanced Materials 28 (41), 9152–9162.

Peng, P., Hu, A., Gerlich, A.P., Zou, G., Liu, L., Zhou, Y.N., 2015. Joining of silver nanomaterials at low temperatures: Processes, properties, and applications. ACS Applied Materials & Interfaces 7 (23), 12597–12618 PMID: 26005792.

Inoue, N., Yonezu, A., Watanabe, Y., Okamura, T., Yoneda, K., Xu, B., 2015. Prediction of viscoplastic properties of polymeric materials using sharp indentation. Computational Materials Science 110, 321–330.

Bucaille, J.L., Felder, E., Hochstetter, G., Sep 2002. Identification of the viscoplastic behavior of a polycarbonate based on experiments and numerical modeling of the nano-indentation test. Journal of Materials Science 37, 3999–4011.

Butt, H.-J., Cappella, B., Kappl, M., 2005. Force measurements with the atomic force microscope: Technique, interpretation and applications. Surface Science Reports 59 (6), 1–152.

Withers, J.R., Aston, D.E., 2006. Nanomechanical measurements with afm in the elastic limit. Advances in Colloid and Interface Science 120 (1-2), 57–67.

Krämer, G., Griepentrog, M., Bonaccurso, E., Cappella, B., 2014. Study of morphology and mechanical properties of polystyrene–polybutadiene blends with nanometre resolution using afm and force–distance curves. European Polymer Journal 55, 123–134 Supplement C.

Efremov, Y.M., Wang, W.-H., Hardy, S.D., Geahlen, R.L., Raman, A., May 2017. Measuring nanoscale viscoelastic parameters of cells directly from afm force-displacement curves. Scientific Reports 7, 1541.

Fischer-Cripps, A., 2004. A simple phenomenological approach to nanoindentation creep. Materials Science and Engineering: A 385 (1-2), 74–82.

Jones, C.A., Grasley, Z.C., 2011. Short-term creep of cement paste during nanoindentation. Cement and Concrete Composites 33 (1), 12–18.

Oyen, M.L., 2006. Analytical techniques for indentation of viscoelastic materials. Philosophical Magazine 86 (33-35), 5625–5641.

Atkins, A., Tabor, D., 1965. Plastic indentation in metals with cones. Journal of the Mechanics and Physics of Solids 13 (3), 149–164.
Bower, A.F., Fleck, N.A., Needleman, A., Ogbonna, N., 1993. Indentation of a power law creeping solid. Proceedings of the Royal Society of London A: Mathematical, Physical and Engineering Sciences 441 (1911), 97–124.
Lee, E.H., Radok, J.R.M., Sept. 1960. The contact problem for viscoelastic bodies. Journal of Applied Mechanics 27, 438–444.
Hill, R., Storakers, B., Zdunek, A.B., 1989. A theoretical study of the brinell hardness test. Proceedings of the Royal Society of London A: Mathematical, Physical and Engineering Sciences 423 (1865), 301–330.
Montoya, C., Arola, D., Ossa, E., 2017. Time dependent deformation behavior of dentin. Archives of Oral Biology 76, 20–29.
Ossa, E., Deshpande, V., Cebon, D., 2005. Spherical indentation behaviour of bitumen. Acta Materialia 53 (11), 3103–3113.
Roumina, R., Raeisinia, B., Mahmudi, R., 2003. Indentation Creep of Antimonial Lead Alloys. J. Mater. Sci. Lett. 22 (20), 1435–1437.
Fujiwara, M., Otsuka, M., 2001. Indentation Creep of β-Sn and Sn–Pb Eutectic Alloy. Mater. Sci. Eng. A 319–321, 929–933.
De La Torre, A., Adeva, P., Aballe, M., 1991. Indentation Creep of Lead and Lead-Copper Alloys. J. Mater. Sci 26 (16), 4351–4354.
Ogbonna, N., Fleck, N.., Cocks, A.C.., 1995. Transient Creep Analysis of Ball Indentation. Int. J. Mech. Sci 37 (11), 1179–1202.
Sader, J.E., Chon, J.W.M., Mulvaney, P., 1999. Calibration of rectangular atomic force microscope cantilevers. Review of Scientific Instruments 70 (10), 3967–3969.
Sader, J.E., Sanelli, J.A., Adamson, B.D., Monty, J.P., Wei, X., Crawford, S.A., Friend, J.R., Marusic, I., Mulvaney, P., Bieske, E.J., 2012. Spring constant calibration of atomic force microscope cantilevers of arbitrary shape. Review of Scientific Instruments 83 (10).
Cappella, B., Dietler, G., 1999. Force-distance curves by atomic force microscopy. Surface Science Reports 34 (1), 1–104.
Johnson, K.L., 1985. Contact Mechanics. Cambridge University Press.
Lu, L., Dao, M., Kumar, P., Ramamurty, U., Karniadakis, G.E., Suresh, S., 2020. Extraction of mechanical properties of materials through deep learning from instrumented indentation. PNAS 117 (13), 7052–7062.
Oyen, M.L., 2005. Spherical indentation creep following ramp loading. Journal of Materials Research 20 (8), 2094–2100.
Cackett, A.J., Lim, J.J., Klups, P., Bushby, A.J., Hardie, C.D., 2018. Using spherical indentation to measure the strength of copper-chromium-zirconium. Journal of Nuclear Materials.
Jennings, A.T., Li, J., Greer, J.R., 2011. Emergence of strain-rate sensitivity in cu nanopillars: Transition from dislocation multiplication to dislocation nucleation. Acta Materialia 59 (14), 5627–5637.
Giwa, A.M., Liaw, P.K., Dahmen, K.A., Greer, J.R., 2016. Microstructure and small-scale size effects in plasticity of individual phases of al0.7cocrfeni high entropy alloy. Extreme Mechanics Letters 8, 220–228 Complete.
van Breemen, L.C.A., Engels, T.A.P., Klompen, E.T.J., Senden, D.J.A., Govaert, L.E., 2012. Rate- and temperature-dependent strain softening in solid polymers. Journal of Polymer Science Part B: Polymer Physics 50 (24), 1757–1771.
Su, C., Herbert, E.G., Sohn, S., LaManna, J.A., Oliver, W.C., Pharr, G.M., 2013. Measurement of power-law creep parameters by instrumented indentation methods. Journal of the Mechanics and Physics of Solids 61 (2), 517–536.
Huang, C.-C., Wei, M.-K., Lee, S., 2011. Transient and steady-state nanoindentation creep of polymeric materials. International Journal of Plasticity 27 (7), 1093–1102.
Griepentrog, M., Krämer, G., Cappella, B., 2013. Comparison of nanoindentation and afm methods for the determination of mechanical properties of polymers. Polymer Testing 32 (3), 455–460.
Passeri, D., Rossi, M., Tamburri, E., Terranova, M., 2013. Mechanical characterization of polymeric thin films by atomic force microscopy based techniques. Analytical and Bioanalytical Chemistry 405 (5), 1463–1478.
Hufenbach, W., Gude, M., BÃ¶hm, R., Zscheyge, M., 2011. The effect of temperature on mechanical properties and failure behaviour of hybrid yarn textile-reinforced thermoplastics. Materials & Design 32 (8), 4278–4288.
Ferry, J.D., 1980. Viscoelastic Properties of Polymers, 3rd Edition. John Wiley and Sons.
Williams, M.L., Landel, R.F., Ferry, J.D., July 1955. The temperature dependence of relaxation mechanisms in amorphous polymers and other glass-forming liquids. J. Am. Chem. Soc. 77, 3701–3707.
Ngai, K.L., Roland, C.M., 1993. Intermolecular cooperativity and the temperature dependence of segmental relaxation in semicrystalline polymers. Macromolecules 26 (11), 2688–2690.
Gilbert, D.G., Ashby, M.F., Beaumont, P.W.R., Sep 1986. Modulus-maps for amorphous polymers. Journal of Materials Science 21, 3194–3210.